Investigation of the background in coherent J/ψ production at the EIC

Wan Chang,[1,2,*] Elke-Caroline Aschenauer,[2,†] Mark D. Baker,[3,‡] Alexander Jentsch,[2,§] Jeong-Hun Lee,[2] Zhoudunming Tu,[2,4,‖] Zhongbao Yin,[1] and Liang Zheng[5]

[1]*Key Laboratory of Quark and Lepton Physics (MOE) and Institute of Particle Physics, Central China Normal University, Wuhan 430079, China*
[2]*Department of Physics, Brookhaven National Laboratory, Upton, New York 11973, USA*
[3]*Mark D. Baker Physics and Detector Simulations LLC, Miller Place, New York 11764, USA*
[4]*Center for Frontiers in Nuclear Science, Stony Brook, New York 11794, USA*
[5]*School of Mathematics and Physics, China University of Geosciences, Wuhan 430074, China*

(Received 10 August 2021; accepted 6 December 2021; published 27 December 2021)

Understanding various fundamental properties of nucleons and nuclei is among the most important scientific goals at the upcoming Electron-Ion Collider (EIC). With the unprecedented opportunity provided by the next-generation machine, the EIC might provide definitive answers to many standing puzzles and open questions in modern nuclear physics. We investigate one of the golden measurements proposed at the EIC, which is to obtain the spatial gluon density distribution within a lead (Pb) nucleus. The proposed experimental process is the exclusive J/ψ vector-meson production off the Pb nucleus: $e + \mathrm{Pb} \to e' + J/\psi + \mathrm{Pb}'$. The Fourier transformation of the momentum transfer $|t|$ distribution of the coherent diffraction is the transverse gluon spatial distribution. In order to measure it, the experiment has to overcome an overwhelmingly large background arising from the incoherent diffractive production, where the nucleus Pb′ mostly breaks up into fragments of particles in the far-forward direction close to the hadron-going beam rapidity. We systematically study the rejection of incoherent J/ψ production by vetoing products from these nuclear breakups—protons, neutrons, and photons—which is based on the BeAGLE event generator and the most up-to-date EIC Far-forward Interaction Region design. The achieved vetoing efficiency, the ratio between the numbers of vetoed events and total incoherent events, ranges from about 80% to 99% depending on $|t|$. Assuming a 5% smearing applied to the reconstructed $|t|$ resolution in the Sartre model, this vetoing efficiency can suppress the incoherent background to at least the first minimum of the coherent $|t|$ distribution. Experimental and accelerator machine challenges as well as potential improvements are discussed.

DOI: 10.1103/PhysRevD.104.114030

I. INTRODUCTION

The future U.S.-based Electron Ion Collider (EIC) [1] will be capable of colliding electrons with a range of ions—from protons to uranium—over a broad range of energies and at very high luminosity (10^{33-34} cm^{-2} sec^{-1}). Additionally, the EIC will enable collisions of polarized electrons and light ions (p, ^{3}He), as it is the only collider in the world with this capability. The EIC will enable study of quantum chromodynamics (QCD) and the imaging of the quarks and gluons, and their interactions in QCD, at a previously unattainable level of precision [2]. The EIC will open up the unique opportunity to go far beyond the present one-dimensional picture of nuclei and nucleons, where the composite nucleon appears as many fast-moving (anti)quarks and gluons whose transverse momenta or spatial extent is not resolved. Specifically, correlating the information of the longitudinal momentum of quarks and gluons with their transverse momentum and spatial distribution inside the nucleon will enable nuclear femtography. Such femtographic images will provide, for the first time, insight into the QCD dynamics inside hadrons, such as the interplay between sea quarks and gluons. Investigating gluons in nuclei instead of protons has multiple advantages; namely, that nuclei act as an effective "amplifier" of phenomena related to high gluon densities, which enhance the impact of nonlinear gluon interactions which possibly lead to gluon saturation [3], also known as the color glass condensate [4–8]. The EIC has the potential to map the transition from a linear to a nonlinear regime in QCD and characterize the relevant parameters governing this transition.

One of the golden measurements proposed at the EIC is the detection of coherent and incoherent vector-meson (VM)

*changwan@mails.ccnu.edu.cn
†elke@bnl.gov
‡mdbaker@bnl.gov
§ajentsch@bnl.gov
‖zhoudunming@bnl.gov

production from heavy nuclei [2]. This measurement has three important physics implications. Coherent production is: (i) a direct measurement of the parton spatial distribution inside of a nucleus, (ii) sensitive to nonlinear dynamics in QCD [2,9–11] when one compares the production of different VMs in different kinematic regions, and (iii) according to the Good-Walker picture [12], the incoherent cross section is a direct measure of the lumpiness of the gluon distribution in the ion.

Like single-slit diffraction in optical experiments, the coherent diffractive production of vector mesons in high-energy experiments is directly sensitive to the size of the target. The most promising channel to map the spatial gluon distribution in nuclei is to measure coherent J/ψ production off a heavy nucleus, such as lead (Pb), where the scattered Pb nucleus is required to stay intact, as described in the reaction process, $e + \mathrm{Pb} \to e' + J/\psi + \mathrm{Pb}'$. The gluon density distribution in transverse impact-parameter space is related by a Fourier transformation with the distribution of the momentum transfer $|t|$ [10] as follows:

$$F(b) = \frac{1}{2\pi}\int_0^\infty d\Delta \cdot \Delta J_0(\Delta b)\sqrt{\frac{d\sigma_{\mathrm{coherent}}}{d|t|}(\Delta)}\Big|_{\mathrm{mod}}. \quad (1)$$

Here $F(b)$ is the gluon density distribution as a function of impact parameter b, $\Delta = \sqrt{-t}$, J_0 is the Bessel function, and $d\sigma_{\mathrm{coherent}}/d|t|$ is the coherent differential cross section. It is critical for the proposed measurement to unambiguously identify the coherent process and measure its differential cross section as a function of $|t|$. In addition, for the same gluon density distribution in a saturated regime, using different VM probes may result in different coherent cross sections, leading to different measured gluon density distributions [10]. However, given the mass of the J/ψ particle, the predicted sensitivity to saturation effects in coherent J/ψ production is smaller than that in lighter mesons, such as ϕ [11], which makes J/ψ a reasonable baseline. In order to probe saturation dynamics, e.g., its impact on gluon distributions, a comparison of ϕ mesons with respect to the J/ψ in coherent production will be essential.

However, the competing process of exclusive incoherent vector-meson production, $e + \mathrm{Pb} \to e' + J/\psi + X$, occurs when the primary interaction takes place at the nucleon level instead of the nucleus. The nucleus could then be broken up by the virtual photon (or the color dipole [9]) into nuclear remnants and nucleons, where individual nucleons stay intact with very small scattering angles. Since the target size between a Pb nucleus (~8 fm) and a nucleon (~0.8 fm) differs by 1 order of magnitude, the resulting distribution of the momentum transfer $|t|$ is expected to be drastically different. The Fourier transformation of the coherent $|t|$ distribution provides the spatial distribution of gluons in the nucleus [10,13], while the target nucleon size is reflected by the incoherent contribution [14,15]

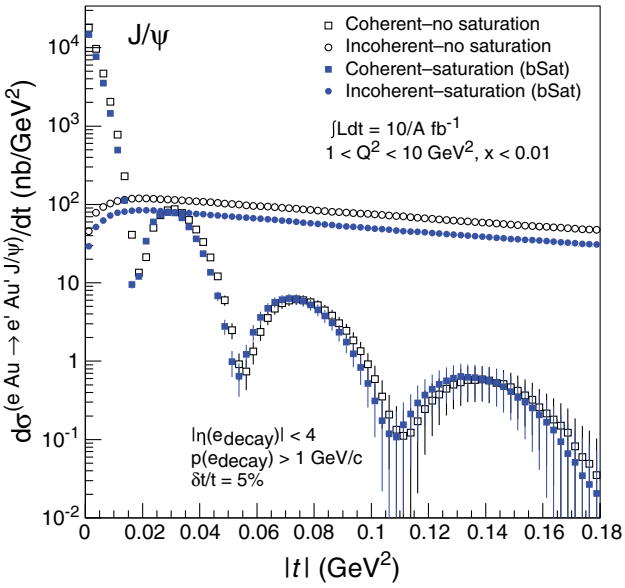

FIG. 1. Differential cross sections of J/ψ production in e-Au collisions at the EIC based on the Sar*t*re model [10]. Both coherent and incoherent production with and without the saturation effect are shown.

dominating for $|t| > 0.015$ GeV^2, as shown in Fig. 1 for the Sar*t*re model simulation [10,16]. Note that the Sar*t*re model uses the gold (Au) nucleus instead of the Pb one, while the difference between the two nuclei is expected to be small relative to other uncertainties.[1] From a recent quantitative study in the EIC Yellow Report [17], resolving the three diffractive minima of the coherent $|t|$ distribution is critical to achieve the goal of this measurement with reasonable precision on the gluon density distribution. In order to observe the three minima from low to high $|t|$ at the EIC, the required vetoing efficiency, the ratio between the numbers of vetoed events and total incoherent events, is roughly 90%, 99%, and > 99.8%, respectively. The three diffractive minima are also shown in Fig. 1, where a 5% resolution effect was included in generating the $|t|$ distributions.

Similarly, at the Relativistic Heavy-Ion Collider (RHIC) and the Large Hadron Collider (LHC), efforts to measure the gluon density distributions of heavy nuclei have already begun using photoproduction of ρ^0 and J/ψ mesons in ultraperipheral collisions (UPCs) [18–25]. These measurements are very similar to the proposed measurement at the EIC, except that the photon virtuality is close to zero in UPCs and one has less control on the event-by-event kinematics. An experimental hint of coherent production has been observed in photoproduction of the ρ^0 meson at RHIC using the STAR detector in Au-Au UPC events [21]. However, in these data the coherent $|t|$ distribution could be

[1] e-Pb collisions are not currently available in the released version of the Sar*t*re model simulation.

strongly contaminated by incoherent contributions, where an additional smearing of up to 10% at low $|t|$ by the photon transverse momentum (photon $p_T \approx 20$–40 MeV$/c$) [26] could be present. These results therefore cannot be used to extract a precise gluon density distribution [21]. Rejecting incoherent contributions in UPC data with an event-by-event experimental method is extremely challenging, if not impossible, since the zero-degree calorimeter (ZDC) is the only available far-forward detector at STAR during heavy-ion collisions. Therefore, the UPC data at RHIC and at the LHC, as of now, cannot achieve the goal of measuring the gluon density distribution in a heavy nucleus, while the planned EIC experiments with their unique detector capabilities along the beam line might have the best opportunity to fulfill this experimental quest in the future.

In this paper, we characterize the dominant background contribution of the coherent J/ψ vector-meson production in e-Pb collisions at the top EIC energy $\sqrt{s} = 89$ GeV. Specifically, we use the BeAGLE event generator to simulate incoherent diffractive J/ψ events, where each event consists of the produced J/ψ at midrapidity, and all the particles from the nuclear breakup at forward rapidities. The final-state particles produced by the nuclear breakup can be any combination of protons, neutrons, photons, and nuclear remnants. These BeAGLE Monte Carlo (MC) events are processed in a GEANT-based simulation of the EIC interaction region (IR) and its far-forward (FF) detectors in order to investigate their acceptances and the impact of beam-related effects. Since the BeAGLE generator does not predict the coherent J/ψ vector-meson production [27], we adopt the ratio of the incoherent to coherent cross section from the Sar*t*re model to define the position and relative magnitude of the three diffractive minima. An event is considered vetoed if there is at least one particle detected in any of the FF detectors. The goal of this study is to see how many events can be vetoed given the current IR and FF detectors using the most up-to-date full detector simulations. The results will provide valuable insight into the detector proposal and future IR improvements at the EIC.

This paper is organized as follows. In Sec. II, the event generator BeAGLE will be briefly introduced. In Sec. III, the forward detectors along the outgoing hadron beam will be discussed. In Sec. IV, the final results will be shown, followed by a discussion of the remaining issues and challenges faced by this measurement in Sec. V. Finally, a summary will be given in Sec. VI.

II. BeAGLE

BeAGLE is a general-purpose electron-nucleus event generator for high-energy eA collisions. It has been extensively used to understand eA physics and the EIC detector/interaction region design [17]. The core of the BeAGLE model is based on the PYTHIA6 event generator [28] for simulating the parton level interactions in electron-nucleon collisions. The nuclear geometry is modeled within a Glauber-type formalism. Final-state interactions between produced particles and spectator nucleons are provided by the program of DPMJET [29]. Finally, the FLUKA model [30,31] is implemented to describe the breakup of the excited nucleus. Below, only the few important features of the BeAGLE model that are most relevant to this paper are described. For details, see Refs. [27,32].

BeAGLE uses a Woods-Saxon distribution for nucleons in heavy nuclei. A Glauber-type multiple scattering formalism is applied to the scattering on the nuclear target, although only one hard $\gamma^* + N$ interaction per event is allowed. Final-state interactions are modeled through the DPMJET [29] intranuclear cascade (INC) process [33], which describes the secondary interactions among the spectator nucleons and the products from the primary electron-nucleon scattering. This is implemented using a formation time τ: the average time needed for creating a secondary particle that might interact with other nucleons. The average hadron formation time τ is defined as follows [34,35]:

$$\tau = \tau_0 \frac{E}{m} \frac{m^2}{m^2 + p_\perp^2}, \tag{2}$$

where E, m, and $p_\perp$ are the energy, mass, and transverse momentum of the secondary particle, respectively. For generating a secondary particle, a particular formation time T is randomly sampled from an exponential distribution, $e^{-T/\tau}$, where τ is the average formation time. Hadrons with higher energy or smaller transverse mass are more likely to have a longer formation time and less likely to be formed inside the nucleus. Note that the parameter τ_0 is a free parameter which has been tuned by comparing it to experimental data. The observable that was used, which is sensitive to the τ_0 parameter, is the average number of neutrons $\langle N_n \rangle$ produced during the evaporation process. We tuned to the multiplicity data of neutron emission in μ-Pb collisions from the E665 experiment at Fermilab [36].

BeAGLE does not simulate coherent diffraction from the entire nucleus, while the E665 data do have coherent diffractive events which do not produce neutrons in the final state. In order to properly tune the τ_0 parameter, a weight is needed for the BeAGLE model to take into account the coherent cross section in the data. The comparison of BeAGLE to the E665 data requires the introduction of the fraction of coherent events over the total cross section $f = N_{\text{coherent}}/N_{\text{total}}$ as follows:

$$N_n(\text{E665}) = 0 * f + N_n(\text{BeAGLE}) * (1 - f). \tag{3}$$

By using this relation, we find the $\tau_0 = 6$ fm for $f = 0.42$, 10 fm for $f = 0.24$, and 14 fm for $f = 0.08$. The default BeAGLE τ_0 is set at 10 fm, while the other two

are served as model uncertainties in estimating the rejection power in the incoherent events. See the details in Appendix A.

In addition, two aspects of nuclear shadowing [37] have been implemented in BeAGLE. First, the cross section for all of the hard interactions is affected by a modification in the parton distribution for the bound nucleons. Second, multinucleon scattering according to a Glauber model is available in BeAGLE, with three possible settings. For the first setting, i.e., $genShd = 1$, it is assumed that one and only one nucleon participates in the hard interaction with the virtual photon. For $genShd = 3$, the photon interacts with multiple nucleons and only one of the struck nucleons is selected randomly to undergo the inelastic interaction. The rest of photon-nucleon interactions are treated as elastic. For $genShd = 2$, the process is the same as $genShd = 3$ except that the order is fixed in a way that the first interaction is always inelastic and the rest is elastic. For tuning the τ_0 parameter, the *genShd* value is set at 3. Using different settings in the nuclear shadowing model has a negligible effect on the E665 evaporation neutron results.

Finally, for incoherent J/ψ production from nuclei, e.g., Pb, the primary interaction is based on the electroproduction of J/ψ as modeled in PYTHIA6. The active nucleon in the BeAGLE event generator can be either a proton or a neutron. For the case of the neutron, the BeAGLE model assumes isospin symmetry for the parton distributions. BeAGLE uses nuclear parton distribution functions for the basic electron-nucleon hard cross section. For these results, the EPS09 parametrization [38] was used. After the hard interaction, the leading nucleon can stay intact (elastic on nucleon level) or dissociate (inelastic on nucleon level) given by two separate processes modeled in PYTHIA6; namely, subprocesses 91 and 93, respectively.

In the measurement of coherent J/ψ production at the EIC, these two processes of incoherent production are the main contributions of the physics background. The resulting final-state products in these processes are therefore the main focus of this paper, and they will be produced mostly in the very forward pseudorapidity region at the EIC. For a similar process in light nuclei, e.g., deuterons; see Ref. [32] for details.

The BeAGLE simulation used in this paper is based on a sample of $e + \mathrm{Pb} \to e' + J/\psi + X$ with 18 GeV electrons scattering off 110 GeV per nucleon Pb nuclei. To date, 1.3×10^6 events of incoherent J/ψ production have been simulated.

III. FAR-FORWARD DETECTORS

The current EIC IR and far-forward region designs are based on the EIC Conceptual Design Report (CDR) [1]. The IR used in this study is located at the six o'clock position (IP6) of the current RHIC complex at BNL, which is the current location of the STAR detector. The FF detectors considered in this study are advanced concepts

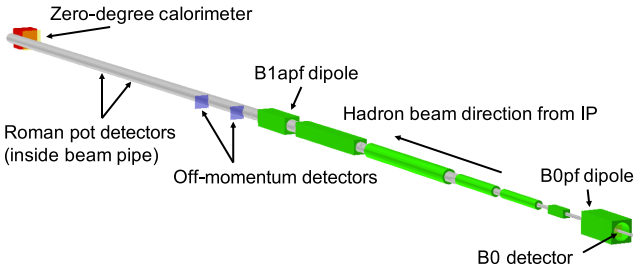

FIG. 2. The layout of the EIC far-forward IR region including the seven dipole and quadrupole magnets for the outgoing hadron beam direction and the four detector subsystems for proton and neutron tagging. The image was generated using EICROOT [39] and GEANT4 [41].

for measuring forward-going particles that are outside the main detector acceptance ($\theta > 35$ mrad) and are based on the EIC reference detector detailed in the EIC Yellow Report [17]. Some general considerations used to establish baseline particle acceptances and detector resolutions for this study via full simulations in EicRoot [39] and GEANT [40,41] are presented here.

In Fig. 2, the layout of the EIC far-forward region at IP6 is shown. The dipole magnets are represented by the green rectangular boxes; the quadrupole magnets, which are used to focus the hadron beams, are represented by the green cylindrical boxes. The gray cylindrical tube represents a simplified preliminary estimate for the beam pipe. In order to tag the maximum number of final-state particles in the FF region, four detector subsystems are employed, each with a different area of geometric acceptance coverage. The FF region, in general, covers a polar angle acceptance of 0–20 mrad and provides coverage for particles of different rigidity (momentum divided by charge) than the beam (so-called off-momentum particles). The position, geometric dimensions, and angular acceptances of these far-forward detectors are summarized in Table I.

Starting at the interaction point and moving downstream, the first detector subsystem is the B0 spectrometer. The B0 system comprises four silicon tracking layers spaced evenly along the majority of the bore length and allows for tagging and reconstruction of charged particles in a ~1.3 T dipole field, enabling reconstruction of particle momentum. Additionally, a preshower detector, consisting of an 11.6 mm (2 radiation length) thick lead layer and a 0.3 mm silicon layer, was included in the B0 magnet bore and after the silicon tracking planes. The entire B0 spectrometer subsystem is designed to tag particles with scattering angles between ~6 and 20 mrad, with the lower bound determined by the size of the hadron beam pipe in the magnet bore ($r = 3.2$ cm), and the upper bound determined by the aperture (bore size) of the magnet.

The next detector subsystem is the so-called off-momentum detector (OMD). In this study, the layout of the OMD was identical to that used in the EIC Yellow

TABLE I. Summary of the physical location and maximum polar angular acceptance for the four far-forward detectors [17].

Detectors	(x, z) positions (m)	Dimensions	θ (mrad)	Notes
B0 tracker	$(x = 0.19,\ 5.4 < z < 6.4)$	(26 cm, 27 cm, not applicable)	$5.5 < \theta < 20$	13 mrad at $\phi = \pi$
Off-momentum	(0.8, 22.5), (0.85,24.5)	(30 cm, 30 cm, not applicable)	$0 < \theta < 5.0$	40%–60% rigidity
Roman pots	(0.85, 26.0), (0.94, 28.0)	(25 cm, 10 cm, not applicable)	$0 < \theta < 5.0$	10σ cut
ZDC	(0.96, 37.5)	(60 cm, 60 cm, 2 m)	$0 < \theta < 5.5$	~4.0 mrad at $\phi = \pi$

Report. The OMD comprises two silicon planes, spaced 2 m apart, and placed just after the B1apf dipole magnet outside the beam pipe vacuum. This subsystem is responsible for capturing protons (or other charged particles), which have a lower magnetic rigidity than the heavy-ion beam, from nuclear breakup. The lower magnetic rigidity causes these charged particles to experience a larger bending angle in the dipole magnets, prompting them to be steered out of the beam pipe. Some further optimizations of the off-momentum detectors are currently under consideration but not yet available. The OMD subsystem covers a polar angle acceptance of 0–5 mrad and accepts particles between roughly 30% and 60% of the beam rigidity.

The third detector subsystem is the Roman pot (RP) silicon detectors. The RP subsystem consists of two stations of silicon planes, spaced 2 m apart, which are injected directly into the beam vacuum a few millimeters from the hadron beam. In other implementations of the RP concept, a metal vessel (the "pot") with a thin window is used to house the detector packages such that the vessel sits in the machine vacuum, while the silicon detectors are outside the vacuum and protected by the pot. In order to maximize the acceptance at lower transverse momentum, the simulations used in this study assume a "potless" design, with the silicon detectors placed directly in the machine vacuum. The RP system nominally accepts particles between 0 and 5 mrad, with a rigidity of between 60% and 100%. However, the detector cannot be placed arbitrarily close to the beam. The safe distance is generally defined as a "rule-of-thumb" 10σ distance, where σ is the transverse beam size and is calculated based on the emittance (ϵ), beta functions (β), momentum dispersion (D), and momentum spread ($\Delta p/p$) of the beam, as shown in Eq. (4),

$$\sigma_{x,y} = \sqrt{\epsilon_{x,y}\beta(z)_{x,y} + D_{x,y}\frac{\Delta p}{p}}. \tag{4}$$

For the beam conditions detailed in the EIC CDR [1] and used in the present simulations, 1σ is a few millimeters in x, and less than a millimeter in y. The transverse beam size at the RP detectors can be altered using different beam optics configurations, which trade off acceptance at the detector and overall luminosity.

The final detector subsystem is the ZDC, which sits just before the B2pf dipole magnet at the end of the drift region. Note that the B2pf dipole magnet is not shown in Fig. 2. The full detector will include both electromagnetic and hadronic calorimetry, with high resolution ($\frac{\Delta E}{E} = \frac{50\%}{\sqrt{E}} \oplus 5\%$ and $\frac{\Delta\theta}{\theta} = \frac{3\ \text{mrad}}{\sqrt{E}}$, where E represents the energy deposition in units of GeV) facilitated by high granularity and large length (2 m) for shower development. The ZDC used for this study did not have the full implementation included, and instead used a plane for detecting the generic neutral particle acceptance, with the resolutions applied as an afterburner to the generator-level particle kinematics. The ZDC can accept neutrons and photons with polar angles between 0 and 4.5 mrad.

The beam pipe used in these simulations is based on a preliminary design with basic assumptions and minimal optimization. The final optimized vacuum engineering design for the first EIC interaction region (IP6) is still under way. Multiple beam pipe materials (beryllium, aluminum, and stainless steel) were considered for their impact on vetoing efficiency, which will provide crucial input to the engineers designing the final vacuum system.

The coordinate system is defined with the z axis in the hadron-going beam direction, the x axis determines the position along the floor transverse to the beam (with positive x following the direction of the dipole bending), and the y axis is the elevation. All detector and beam-lattice components are at the same elevation (i.e., same y coordinate), with the details available in the EIC CDR [1].

IV. RESULT

In this section, we investigate the background contribution to exclusive coherent J/ψ production from the incoherent process, i.e., $e + \text{Pb} \to e' + J/\psi + X$. In fact, this process is the dominant background contribution for most of the range of the momentum transfer $|t|$. In order to suppress the incoherent process, the final-state particles would have to be detected event by event using forward particle detectors. In the BeAGLE model, the incoherent J/ψ is produced together with one or more ions and, as shown in Table II, protons, neutrons, photons, or any combination of them, depending on the excitation energy. Most events have more than one such particle produced, while around 10% of events have only either neutrons or photons. Only one particle is needed to be detected for a

TABLE II. Summary of particles produced in incoherent J/ψ production in BeAGLE.

Produced particle	Rate
Only neutron	7.66%
Only proton	0%
Only photon	3.25%
Neutron and proton	3.19%
Neutron and photon	44.24%
Proton and photon	2.27%
Neutron, proton and photon	39.39%

successful veto, so naturally events with fewer particles are generally more difficult to veto.

In Fig. 3, the two-dimensional distributions of scattering angle θ and the total momentum p of protons, neutrons, and photons are shown for the process of incoherent J/ψ production in e-Pb collisions with 18 GeV on 110 GeV at the EIC. Based on single particle distributions, neutrons are found to have an acceptance × efficiency of close to 75% within a 5 mrad cone of the scattering angle. Most of the inefficiency is due to the neutrons having already begun showering in the beam pipe (see details later). For protons, the acceptance is generally very good except at very large scattering angles and very low momenta. The three different proton detectors cover almost the entire phase space in the scattering angle up to 22 mrad. Because of the rigidity change, the RPs have an insignificant contribution, while the OMDs and the B0 detectors accept 31% and 16% of the protons, respectively. Photons with an energy above 50 MeV and a scattering angle less than 5 mrad can be detected by the ZDC. This results in a 16% acceptance. Most of the photons have a scattering angle outside the ZDC acceptance. Therefore, a preshower detector is included in the set of detectors to be installed on the B0 magnet bore to detect the photon with a scattering angle greater than 5 and less than 22 mrad. Note that protons and neutrons with a very low momentum and very large scattering angle are mostly the primary nucleon participating in the hard scattering or are products of the INC. However, in most cases, these particles are produced in coincidence with other breakup particles within the detector acceptance; therefore, the events can be efficiently vetoed.

For a successful veto of incoherent diffractive events, detection of one particle is sufficient. Therefore, the remaining background events will have none of the veto requirements fulfilled. In order to detail the vetoing procedure step-by-step, we break them down to selections on different particles in different detectors, listed as follows:

(a) Veto.1: no activity other than e^- and J/ψ in the main detector ($|\eta| < 4.0$ and $p_T > 100$ MeV/c).
(b) Veto.2: veto.1 and no neutron in ZDC.
(c) Veto.3: veto.2 and no proton in RP.
(d) Veto.4: veto.3 and no proton in OMDs.
(e) Veto.5: veto.4 and no proton in B0.
(f) Veto.6: veto.5 and no photon in B0.
(g) Veto.7: veto.6 and no photon with $E > 50$ MeV in ZDC.

In Fig. 4, the incoherent J/ψ production $dN/d|t|$ as a function of momentum transfer $|t|$ based on the BeAGLE event generator is shown. The total number of events before any vetoing is shown as a black solid line; the other colored lines indicate the results after different vetoing requirements are applied. The results for cuts that have a negligible impact on the vetoing are not shown in the figure. The uncertainty bands are based on different results obtained by varying the τ_0 parameter, from 6 to 14 fm, with 10 fm used as the central value. The vetoing efficiency with different τ_0 values is found to be similar, where the fraction of the total surviving events after veto.7 is 1.98% for $\tau_0 = 6$ fm, and 2.14% for $\tau_0 = 14$ fm, respectively. Therefore, the quoted uncertainty is less than 0.1%. No detailed studies on the vetoing power of the EIC central detector have been performed, as the detector layouts are still being developed.

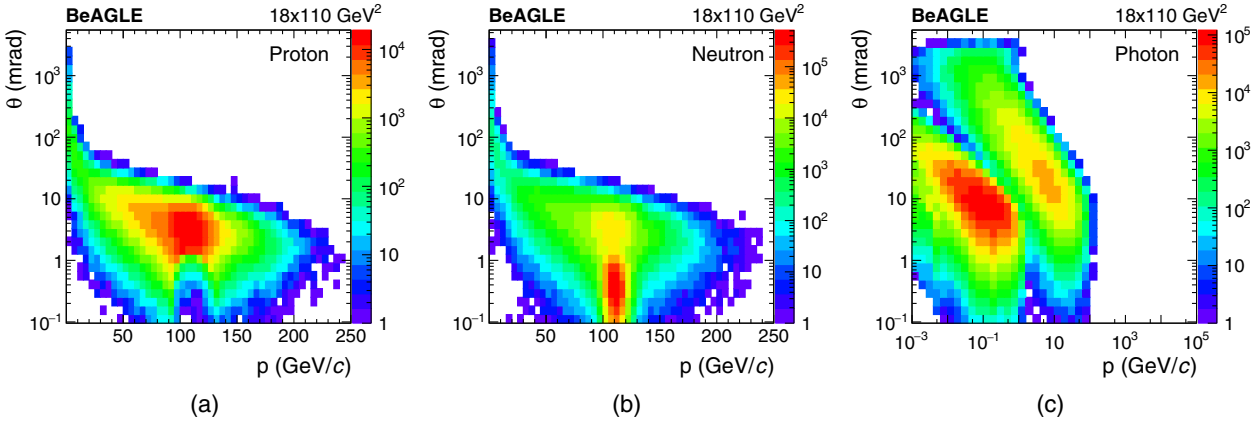

FIG. 3. The scattering angle as a function of the total momentum of (a) protons, (b) neutrons, and (c) photons for incoherent events before any veto was applied.

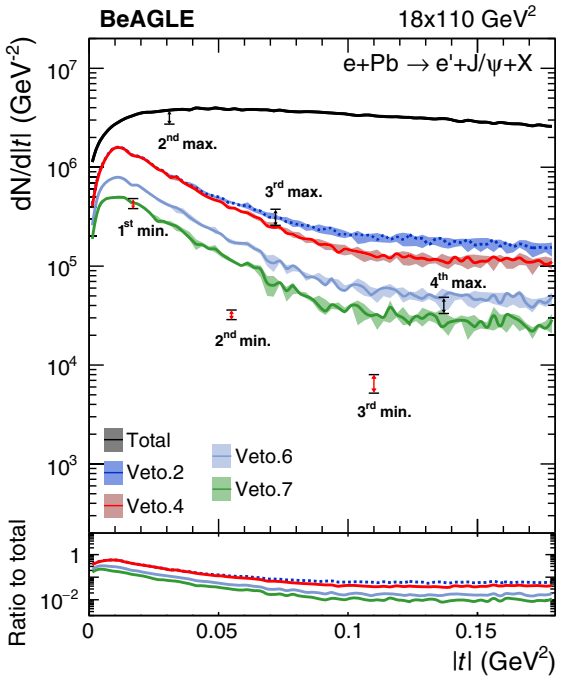

FIG. 4. Distribution of the momentum transfer $|t|$ for incoherent J/ψ production in e-Pb collisions with 18 GeV on 110 GeV at the EIC. Different lines indicate results after different vetoing requirements. The magnitude and position of the three coherent diffractive minima and maxima based on the $|t|$ distribution from Sar*t*re are indicated. The size of the arrow indicates the difference assuming a saturation and a nonsaturation model.

Nevertheless, vetoing particles with $|\eta| < 4.0$ and $p_T > 100$ MeV/c other than the scattered electron e^- and J/ψ has a very small impact because no other event categories, i.e., deep inelastic scattering, were included in this study. Figure 4 shows that vetoing on protons, neutrons, and photons is all important and contributes to a significant reduction of the background. After veto.7, the residual contribution is about 1%–20% of the total events, depending on the value of $|t|$. For veto.7, we set a 50 MeV cut as the minimum detection energy of the photons. Detecting such low-energy photons in the ZDC above background is challenging; therefore, we also investigate the effect of a higher cut of 100 MeV. A photon cut of 100 MeV would lead to the fraction of surviving events after veto.7 of about 2.18% of the total events vs 2.05% for the default 50 MeV cut, as shown in Table III in Appendix B.

Furthermore, the relative magnitude and position of the three coherent diffractive minima with an assumed 5% smearing applied to the reconstructed $|t|$ distribution from Sar*t*re [10] are shown in Fig. 4 as red arrows. The difference between the upper and lower bars indicates the difference assuming a saturation and a nonsaturation model [10]. Similarly, the relative magnitude and position of the second through fourth maxima (the first maximum is at or near zero) are shown as black arrows. Even though the result from the Sar*t*re model is for e-Au collisions and the BeAGLE study in this paper uses e-Pb collisions, they are close enough to make this comparison. If one wants to reach the three minima as required to image the parton spatial distribution inside of a nucleus, we find that the vetoing efficiency needed is around 99.8% at the t location of the third minimum. The current result shown in Fig. 4 is found to be just enough to reach the first minimum, where the required vetoing efficiency is about 90%. Based on the Yellow Report [17] study, if the background to the level of these minima is not suppressed, the Fourier transformation to obtain the gluon density distributions is significantly smeared. Thus far, with the current forward interaction region design and the BeAGLE model, there is at least a factor of 4 or more suppression needed to reach the second and third minima.

The scattering angle θ vs total momentum p after veto.7 for protons, neutrons, and photons of the residual events are shown in Fig. 5. The inset in each panel shows the particle multiplicity distributions both before and after vetoing.

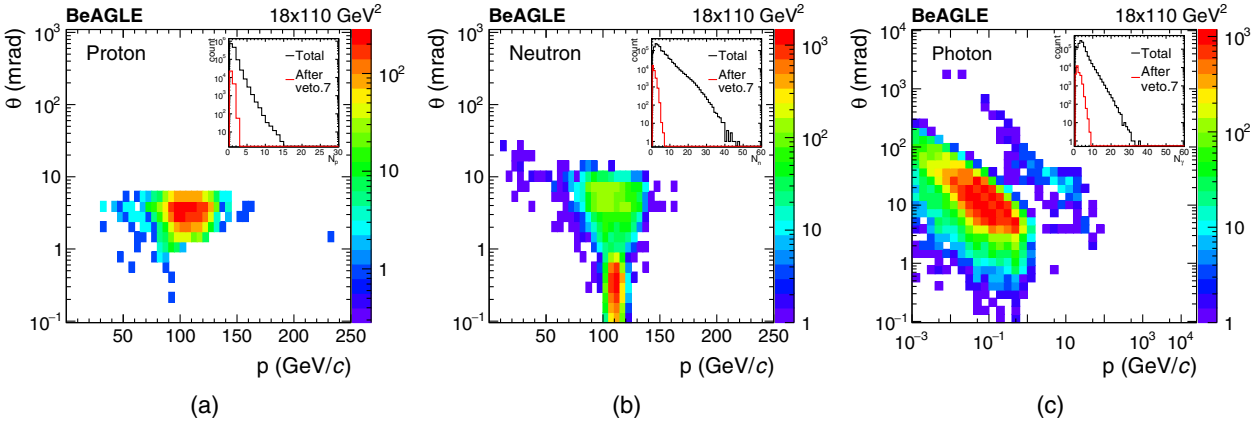

FIG. 5. The scattering angle as function of the total momentum for (a) protons, (b) neutrons, and (c) photons after veto.7. Insets: particle multiplicity distributions for both the MC truth level (total) and after applying all cuts to veto the incoherent events.

The vetoing efficiencies for neutrons, protons, and photons are over 99%. The dominant residual particle among the three is the photon, especially photons with very low energy. The multiplicity of the surviving events is peaked at low multiplicity because the more particles there are in a single event, the more likely it can be vetoed. High multiplicity events are also more likely to have soft particles, which are farther away from the nominal beam momentum. These particles are more easily vetoed; therefore, high multiplicity events are almost always rejected.

The surviving events not only have low particle multiplicity but also contain high mass nuclear remnants (e.g., for Pb with A = 208, 207, 206, etc.) with momenta close to the beam. The mass number distribution for nuclei of total and surviving events after veto.7 is shown in Fig. 6(a).

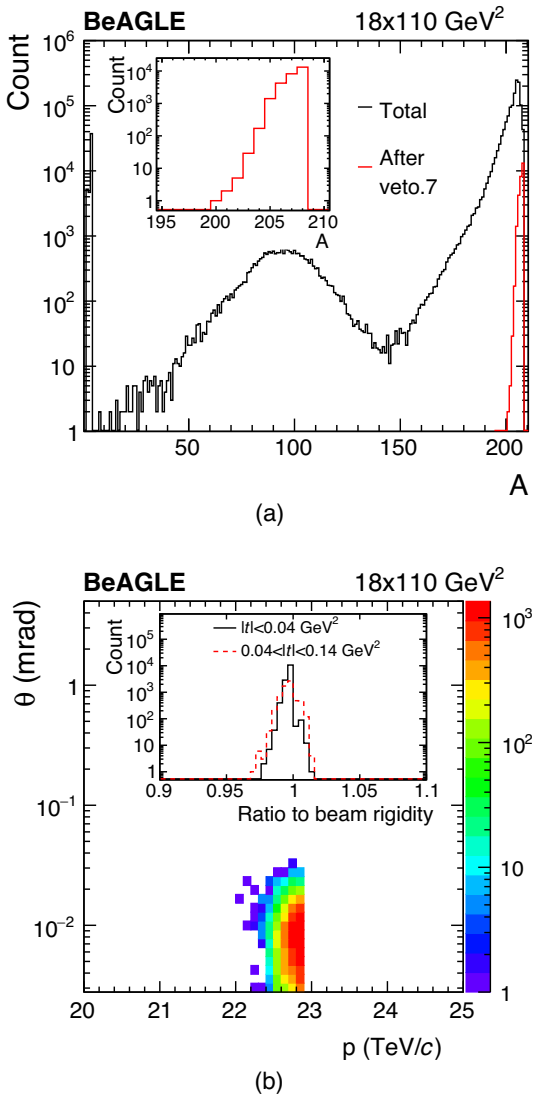

FIG. 6. (a) The mass number distribution for nuclei of total and surviving events after veto.7. (b) The scattering angle versus total momentum for nuclei of surviving events after veto.7. Inset: ratio of the residual nuclei rigidity to that of the nuclear beam.

Examining the residual events, one finds that the mass number A is greater than 200 and peaks at 208, which is primarily due to events with only photon emission from an excited Pb^{208} nucleus. Figure 6(b) shows the scattering angle as a function of the total momentum of the nuclei for these residual events; the momentum is large and the scattering angle is less than 0.05 mrad. The rigidity change of these nuclei is presented as the ratio with respect to the beam rigidity; see the inset of Fig. 6(b). The black solid line shows the distribution of events with momentum transfer $|t|$ less than 0.04 GeV^2 and the red dashed line is for events with $0.04 < |t| < 0.14$ GeV^2. The ratio for both $|t|$ ranges is between 0.97 and 1.03, which makes it extremely difficult to detect. Based on these numbers, these nuclei will remain in the envelope of the beam at IP6.

Finally, we have also investigated the impact of the beam pipe on the veto efficiency. The results with and without a beam pipe are shown in Fig. 7. The green line represents the distribution of the residual events, including a beam pipe in the simulation, while the blue line shows the result without a beam pipe. As one can see, without a beam pipe, the t-averaged veto efficiency is close to 99% in total after veto.7 and is found to be enough to reach the first, second, and third minimum of the momentum transfer $|t|$ distribution. We studied also the dependence of the veto efficiency on the beam pipe material. The surviving events after veto.7 with an aluminum beam pipe are 2.46%, which is almost the same as for beryllium. The veto efficiency with stainless steel is found to be significantly lower with 5.58% incoherent events surviving. The current design of the beam pipe is still preliminary; further optimization of the beam pipe material and layout could lead to improvements in the efficiency of detecting the nuclear breakup particles. In short, the beam pipe design is critical to the veto efficiency for the process of interest in this study. For details, see Appendix B for the surviving event ratio after each step for different materials, as shown in Table III.

V. DISCUSSION

A. Model uncertainty

In the prior section, we described the vetoing process of incoherent J/ψ production modeled on the BeAGLE event generator that is experimentally accessible at the EIC. However, the nuclear breakup mechanism, its associated particle production, and their kinematic distributions in eA collisions based on the BeAGLE model have not been rigorously validated against data. As of today, there are no data that can be used for validation. In the near future, the data that might provide insights to this process are UPCs at RHIC and at the LHC run 3. Therefore, there remain some theoretical uncertainties in the BeAGLE model. However, we have systematically checked parameters related to the hadron formation time τ, the results are found to be stable with respect to these model variations.

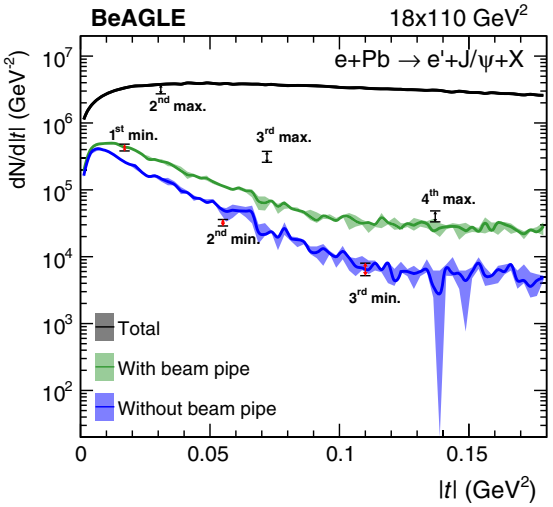

FIG. 7. Distribution of the momentum transfer $|t|$ for incoherent J/ψ production in e-Pb collisions at the EIC (18 GeV on 110 GeV). Different lines indicate the effect of the beam pipe on the vetoing efficiency. The magnitude and position of the three coherent diffractive minima and maxima based on the $|t|$ distribution from Sar*t*re are indicated. The size of the arrow indicates the difference assuming a saturation and a nonsaturation model.

There is another source of uncertainty which comes from the Sar*t*re model. Since the BeAGLE generator predicts only the incoherent J/ψ production, we adopt the ratio of coherent to incoherent cross section from the Sar*t*re model to define the position and relative magnitude of the three minima shown in Figs. 4 and 7. As with BeAGLE, the prediction of incoherent and coherent cross sections from the Sar*t*re generator may have their own model uncertainties, especially for the incoherent production. From a recent study of the Sar*t*re model used describing the UPC data, the agreement was found to be very good [11]. However, the comparison was for the total cross section level without studying the $|t|$ dependence. A more quantitative comparison with the differential cross section data as a function of $|t|$ would be extremely valuable for understanding uncertainties in more detail.

The main results presented in Sec. IV are for the kinematic range Q^2 values greater than 1. In order to estimate the Q^2 dependence and W dependence on the vetoing efficiency, we have also repeated the current analysis for three Q^2 bins, $1 < Q^2 < 2\,\mathrm{GeV}^2$, $2 < Q^2 < 5\,\mathrm{GeV}^2$, and $5 < Q^2 < 10\,\mathrm{GeV}^2$, and four W bins, $W < 20\,\mathrm{GeV}^2$, $20 < W < 40$ GeV, $40 < W < 60$ GeV, and $W > 60$ GeV. The vetoing efficiencies for these variations are found to be similar. This result is expected, as the nuclear breakup is not directly correlated with the hard scattering.

B. Possible instrumental improvements

The results presented in this paper are based on the EIC reference detector and conceptual design of the IP6 IR configuration detailed in the EIC CDR [1]. One goal of this analysis is to give ideas for further optimizing the forward-going particle tagging efficiency and associated veto efficiency for incoherent breakup events from diffractive J/ψ production in eA collisions. Given the current design and layout, one of the most important aspects is the design of the beam pipe and vacuum system. Although a quantitative analysis and careful assessment are needed in order to draw definitive conclusions, our results indicate that an improvement of the vetoing power is possible by further optimizing the beam pipe design. This optimization would include using thin, low density materials in regions where particles exit (e.g., beryllium and aluminum where possible), and the inclusion of an exit window or windows to increase the incident angles for exiting particles, and thereby decrease the effective interaction length. Based on the quantitative impact study in the EIC Yellow Report [17], the suppression of incoherent events to a level close to the three diffractive minima will fulfill the requirement of this measurement, e.g., the reconstruction of the gluon density distribution in the Pb nucleus. Figure 7 shows the momentum transfer $|t|$ with and without the beam pipe included in the simulation. While it is not possible to completely remove the impact of the beam pipe on the vetoing efficiency, efforts are under way to minimize the negative impact of the design and optimize various components (e.g., tapers, exit window) where possible. With a sufficiently optimized design, this measurement could still be feasible at IP6.

In addition, in a recent preliminary design study on the second IR (the eight o'clock position in the RHIC complex: IP8) at the EIC, a different crossing angle and far-forward layout have been proposed than in the IP6 configuration. The current preliminary IP8 concept includes a 35 mrad crossing angle, and the inclusion of a secondary focus farther downstream, which enables a Roman pot system to be installed in a region where the 10σ safe distance is much smaller ($\sim$1 mm or less). The secondary focus makes use of the so-called point-to-point focusing mechanism, which enables optimization of acceptance at low p_T. This enables the reduction of the transverse beam size by an order of magnitude or more relative to the standard location of the Roman pots system at IP6 by forcing the beta functions just after the secondary focus to be similar to the β^* values at the IP. This will lead to a significant improvement in the forward-going particle acceptance in scattering angle and rigidity phase space, allowing some of the particles, and therefore the events shown in Fig. 6(b), to be tagged and vetoed. This proposed capability in the preliminary IP8 design will specifically improve the tagging efficiency of nuclear fragments from the breakup of the heavy nucleus, which are normally well within the 10σ beam envelope at the nominal location of the Roman pots, and therefore undetectable.

In addition to the improvements for detection of low-angle charged particles and nuclear remnants at IP8,

assuming that wider aperture magnets can improve the acceptance of neutrons and photons in the ZDC, potentially up to ~9 mrad in some regions of the azimuthal phase space. Based on the particle distributions of the residual events in Fig. 5, the combination of the improved neutral particle acceptance and the ability to tag more of the charged nuclear remnants could improve the vetoing efficiency.

VI. SUMMARY

We present in this paper an investigation of the background in coherent diffractive J/ψ production using the BeAGLE event generator for 18 GeV electrons scattering off 110 GeV lead nuclei at the EIC. The BeAGLE simulations provide the dominant physics background to the coherent diffractive J/ψ production—the incoherent events. In the BeAGLE model, incoherent J/ψ production processes result in forward-going particles, e.g., protons, neutrons, and photons due to the nuclear breakup. After simulating these events using the most up-to-date design of the EIC interaction region, specifically for the outgoing hadron beam direction and its detectors and a beryllium beam pipe, the total vetoing fraction of these events is found to be 98%. Based on a 5% $|t|$ resolution, this rejection power is found to be just enough to suppress the background events to the first minimum position of the predicted coherent $|t|$ distribution, while more suppression is needed to reach the level of the second and third minima. However, a realistic detector design and its tracking momentum resolution could result in a $|t|$ resolution that is worse than 5%; therefore, the impact of the rejection power found in this study would need to be reassessed. Although an active investigation on other possible instrumental improvements is ongoing within the EIC community, the quantitative study reported in this paper shows for the first time a realistic assessment of realizing this experimental measurement. The method and experimental setup employed in this work will serve as a baseline for future design iterations of the EIC forward IR and its detectors.

ACKNOWLEDGMENTS

We thank T. Ullrich for a discussion on the Sar*t*re model and its prediction for different kinematic ranges in Q^2. We thank C. Hyde, V. Morozov, T. Toll, and P. Turonski for the helpful discussions. We would also like to thank the EIC project interaction region working group for their help in understanding the various impacts of the IR design. The work of W. C. is supported by the U.S. Department of Energy under Contract No. de-sc0012704 and the National Natural Science Foundation of China with Grant No. 11875143. The work of E.-C. A., A. J., and J.-H. L. is supported by the U.S. Department of Energy under Contract No. de-sc0012704, and A. J. is also supported by the development program at Brookhaven National Laboratory. The work of M. D. B. is supported by U.S. DOE Contracts No. de-sc0012704 and No. DE-AC05-06OR23177, and by Jefferson Lab LDRD Project No. LDRD1706. The work of Z. T. is supported by Brookhaven National Lab LDRD Project No. LDRD-18-039, the U.S. Department of Energy under Award No. DE-SC0012704, and the Goldhaber Distinguished Fellowship at Brookhaven National Laboratory. The work of Z. Y. is supported by the National Natural Science Foundation of China under Grant No. 11875143. The work of L. Z. is supported by the National Natural Science Foundation of China under Grant No. 11905188.

APPENDIX A: DETERMINATION OF THE τ_0 PARAMETER IN BeAGLE

In BeAGLE (and in DPMJET), a formation time τ is needed before the secondary particles can be newly created and can interact with other nucleons. It is defined as Eq. (2) in Sec. II. τ_0 is a free parameter which determines the overall scale for the formation length in this equation, and its setting can affect the multiplicity of the neutron emission.

Figure 8 shows the average neutron multiplicity, $\langle N_n \rangle$ vs the fraction of coherent to total events f for a variety of different τ_0 values. The black dashed curve in the plot is constrained by E665 neutron data, and a value of 4.70415 is obtained by a fit to E665 neutron multiplicity as a function of ν for Pb target [36]. After fitting, we found $N_n(\text{E665})$ is independent of ν, which is a constant of 4.70415. From Eq. (3), one can get the result that $N_n(\text{BeAGLE}) = 4.70415/(1-f)$. Different colors represent different τ_0 values, where the black solid lines are the half-integer τ_0 values. For example, the ones between 5 and 6 fm are for $\tau_0 = 5.5$ fm, and the values are similar for others. We use the following settings for the main results: $\tau_0 = 6$ fm ($f = 0.42$), 10 fm ($f = 0.24$), and 14 fm ($f = 0.08$).

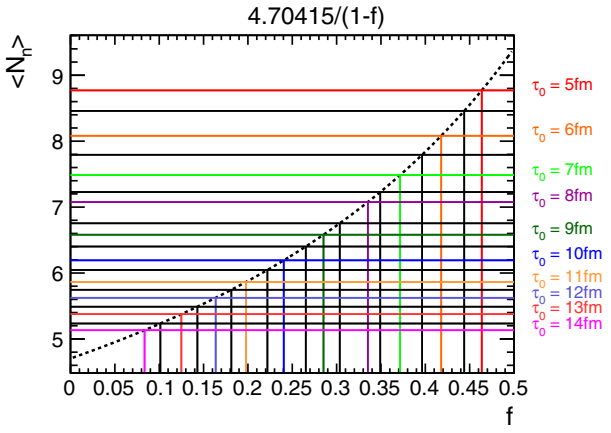

FIG. 8. The average neutron multiplicity $\langle N_n \rangle$ vs f, the ratio of the number of coherent to the total events for different values of τ_0.

The result with $\tau_0 = 10$ fm is used as the central value, while 6 and 14 fm represent the systematic uncertainty.

APPENDIX B: BEAM PIPE MATERIAL STUDY

In this study, a simplified beam pipe design was included in the simulations to quantify the impact on the veto efficiency. A final engineering design was not available at the time of the study for consideration. The beam pipe sections will be in order from the IP to the drift region where the far-forward detectors (RP, OMD, and ZDC) are located. The beam pipe in the B0pf dipole magnet has a radius of 3.2 cm and is made of beryllium with a thickness of 2 mm. This radius was chosen to allow for a 5 mrad cone of protons to pass though unimpeded. The beam pipe sections in the other dipoles and quadrupoles between B0pf and B1apf have the same radii as their respective magnet bores and assume stainless tubes with a 2 mm thickness. The beam pipe in the drift region after the B1apf dipole magnet consists of two sections spanning the full length of the drift region: (i) a straight cylindrical tube with a radius of 20 cm that extends just past the second Roman pot station, (ii) a conical section that tapers from a 20 cm radius to a 7 cm radius at the B2pf magnet entrance. Both sections of the beam pipe between B1apf and B2pf are made of stainless steel with a thickness of 2 mm. However, simulations were also performed using beryllium and aluminum since sections of the pipe where protons, neutrons, and photons exit to stream toward detectors could consist of less dense material sections, modest exit windows, or both. The final design considerations are still under study.

Table III summarizes the step-by-step vetoing power assuming different beam pipe materials. Note that the geometrical layout is identical in all cases. For veto.7, the percentage of survived events with a higher energy cut of 100 MeV for detecting photons is also shown in the bottom row for the beryllium case. This systematic variation is to ensure that our conclusion drawn on the incoherent vetoing is not sensitive to the energy threshold of the photon detection in these kinematic ranges.

TABLE III. Summary of the percentage of events surviving the different vetoing steps for incoherent events assuming no beam pipe and differing beam pipe materials of beryllium, aluminum, and stainless steel.

	Survived event ratio			
Material	Without beam pipe	Beryllium	Aluminum	Stainless steel
Total events	100%	100%	100%	100%
Veto.1	86.9%	86.9%	86.9%	86.9%
Veto.2	5.81%	9.73%	9.85%	17.2%
Veto.3	5.81%	9.73%	9.85%	17.2%
Veto.4	5.09%	8.77%	8.89%	15.73%
Veto.5	4.32%	6.22%	5.97%	10.18%
Veto.6	2.29%	3.32%	3.18%	5.68%
Veto.7 ($E_{\text{photon}} > 50$ MeV)	1.06%	2.05%	2.46%	5.58%
Veto.7 ($E_{\text{photon}} > 100$ MeV)	⋯	2.18%	⋯	⋯

[1] J. Adam *et al.*, https://www.bnl.gov/ec/files/EIC_CDR_Final.pdf (2021).
[2] A. Accardi *et al.*, Eur. Phys. J. A **52**, 268 (2016).
[3] S. Munier, A. M. Stasto, and A. H. Mueller, Nucl. Phys. **B603**, 427 (2001).
[4] F. Gelis, E. Iancu, J. Jalilian-Marian, and R. Venugopalan, Annu. Rev. Nucl. Part. Sci. **60**, 463 (2010).
[5] J. Jalilian-Marian, EPJ Web Conf. **66**, 04012 (2014).
[6] J. Jalilian-Marian and Y. V. Kovchegov, Prog. Part. Nucl. Phys. **56**, 104 (2006).
[7] H. Weigert, Prog. Part. Nucl. Phys. **55**, 461 (2005).
[8] E. Iancu and R. Venugopalan, in *Quark-Gluon Plasma 4*, edited by R. C. Hwa and X.-N. Wang (World Scientific, Singapore, 2003).
[9] H. Kowalski and D. Teaney, Phys. Rev. D **68**, 114005 (2003).
[10] T. Toll and T. Ullrich, Phys. Rev. C **87**, 024913 (2013).
[11] B. Sambasivam, T. Toll, and T. Ullrich, Phys. Lett. B **803**, 135277 (2020).
[12] M. L. Good and W. D. Walker, Phys. Rev. **120**, 1857 (1960).
[13] S. R. Klein, J. Nystrand, J. Seger, Y. Gorbunov, and J. Butterworth, Comput. Phys. Commun. **212**, 258 (2017).

[14] T. Lappi and H. Mantysaari, Phys. Rev. C **83**, 065202 (2011).
[15] A. Caldwell and H. Kowalski, Phys. Rev. C **81**, 025203 (2010).
[16] T. Toll and T. Ullrich, Comput. Phys. Commun. **185**, 1835 (2014).
[17] R. Abdul Khalek *et al.*, arXiv:2103.05419.
[18] V. Khachatryan *et al.* (CMS Collaboration), Phys. Lett. B **772**, 489 (2017).
[19] B. Abelev *et al.* (ALICE Collaboration), Phys. Lett. B **718**, 1273 (2013).
[20] J. Adam *et al.* (ALICE Collaboration), J. High Energy Phys. 09 (2015) 095.
[21] L. Adamczyk *et al.* (STAR Collaboration), Phys. Rev. C **96**, 054904 (2017).
[22] S. Acharya *et al.* (ALICE Collaboration), J. High Energy Phys. 06 (2020) 035.
[23] S. Acharya *et al.* (ALICE Collaboration), Phys. Lett. B **820**, 136481 (2021).
[24] S. Acharya *et al.* (ALICE Collaboration), Phys. Lett. B **817**, 136280 (2021).
[25] S. Acharya *et al.* (ALICE Collaboration), Eur. Phys. J. C **81**, 712 (2021).
[26] J. Adam *et al.* (STAR Collaboration), Phys. Rev. Lett. **127**, 052302 (2021).
[27] E. Aschenauer, M. Baker, W. Chang, J. Lee, Z. Tu, and L. Zheng, https://wiki.bnl.gov/eic/index.php/BeAGLE (2019).
[28] T. Sjöstrand, S. Mrenna, and P. Skands, J. High Energy Phys. 05 (2006) 026.
[29] S. Roesler, R. Engel, and J. Ranft, in *Advanced Monte Carlo for Radiation Physics, Particle Transport Simulation and Applications*, edited by A. Kling, F. J. C. Barö, M. Nakagawa, L. Távora, and P. Vaz (Springer, New York, 2000), pp. 1033–1038.
[30] T. Bhlen, F. Cerutti, M. Chin, A. Fass, A. Ferrari, P. Ortega, A. Mairani, P. Sala, G. Smirnov, and V. Vlachoudis, Nucl. Data Sheets **120**, 211 (2014).
[31] A. Ferrari, P. R. Sala, A. Fasso, and J. Ranft, arXiv:10.2172/877507 (2005).
[32] Z. Tu, A. Jentsch, M. Baker, L. Zheng, J.-H. Lee, R. Venugopalan, O. Hen, D. Higinbotham, E.-C. Aschenauer, and T. Ullrich, Phys. Lett. B **811**, 135877 (2020).
[33] H. W. Bertini, Phys. Rev. **131**, 1801 (1963).
[34] A. Ferrari, P. R. Sala, J. Ranft, and S. Roesler, Z. Phys. C **70**, 413 (1996).
[35] L. Zheng, E. Aschenauer, and J. Lee, Eur. Phys. J. A **50**, 189 (2014).
[36] M. R. Adams *et al.* (E665 Collaboration), Phys. Rev. Lett. **74**, 5198 (1995); **80**, 2020(E) (1998).
[37] L. L. Frankfurt and M. I. Strikman, Phys. Rep. **160**, 235 (1988).
[38] K. Eskola, H. Paukkunen, and C. Salgado, J. High Energy Phys. 04 (2009) 065.
[39] A. Kiselev and A. Jentsch, https://github.com/eic/EicRoot (2020).
[40] R. Brun, F. Bruyant, M. Maire, A. C. McPherson, and P. Zanarini, https://cds.cern.ch/record/1119728 (1987).
[41] S. Agostinelli *et al.* (GEANT4 Collaboration), Nucl. Instrum. Methods Phys. Res., Sect. A **506**, 250 (2003).